Underground Traffic-Induced Body Waves Used to Quantify Seismic Attenuation Properties of a Bimaterial Interface Nearby a Main Fault

Yves Le Gonidec, Bruno Kergosien, J. Wassermann, D. Jaeggi, C. Nussbaum

JGR Solid Earth

RESEARCH ARTICLE
10.1029/2021JB021759

Underground Traffic-Induced Body Waves Used to Quantify Seismic Attenuation Properties of a Bimaterial Interface Nearby a Main Fault

Y. Le Gonidec[1], B. Kergosien[1], J. Wassermann[2], D. Jaeggi[3], and C. Nussbaum[3]

[1]Université de Rennes, CNRS, Géosciences Rennes - UMR6118, Rennes, France, [2]Laboratoire L2MGC, CY Cergy Paris Université, Cergy-Pontoise, France, [3]Swisstopo, Federal Office of Topography, Wabern, Switzerland

Key Points:

- Traffic-induced events in the nearby Mont Terri motorway tunnel are used as reproducible moving seismic sources
- Seismic wave geometric factor and rock material intrinsic attenuation are quantified simultaneously from the ground-borne vibrations
- Different dominant seismic body waves are identified on either side of the Main Fault

Correspondence to:

Y. Le Gonidec,
Yves.LeGonidec@univ-rennes1.fr

Citation:

Le Gonidec, Y., Kergosien, B., Wassermann, J., Jaeggi, D., & Nussbaum, C. (2021). Underground traffic-induced body waves used to quantify seismic attenuation properties of a bimaterial interface nearby a Main Fault. *Journal of Geophysical Research: Solid Earth*, *126*, e2021JB021759. https://doi.org/10.1029/2021JB021759

Received 20 JAN 2021
Accepted 16 JUL 2021

Abstract Underground traffic activities spread ground-borne vibrations in a complex way. The present work focuses on 173 individual vehicles tracked as moving sources of vibrations in the Mont Terri rock laboratory, located 95 m away from a motorway tunnel. Two neighboring geophones record the vertical ground velocity of traffic-induced events with peak particle velocities ranging in 0.15–0.35 μ m/s. A dynamic cross-correlation of the waveforms is used to align the individual events for coherent and robust analysis. A root mean square (rms) method allows identifying the main feature, centered at the Main Fault, and an unexpected feature located about 140 m apart. The dominant seismic frequencies are 15 and 10 Hz, respectively. The vehicle speeds (70–90 km/h), estimated from the time-delay between the two features, and the seismic velocity (800–2,300 m/s), assessed from a simple kinematic model, are used to convert time to position along the tunnel, allowing modeling the local rms with the Bornitz's equation. The resolved frequency-independent attenuation coefficients are 2.61 s/km in the Opalinus Clay including the gallery network, and 1.23 s/km in the Limestone, a contrast of elastic properties that defines a bimaterial interface. A particle motion analysis highlights body waves, with dominant vertically polarized shear waves above the Main Fault. The origin of the unexpected feature is discussed in terms of site effects and seismic propagation in a heterogeneous fracture network. Traffic-induced events can be used as reproducible, low-frequency, and non-destructive sources with potential interest in long-term monitoring at the scale of an underground gallery.

1. Introduction

Natural phenomena, such as storms and earthquakes, and human activities, such as mining, geophysical exploration, road, and railway traffic sources, induce ground vibrations at different strain levels. Ground-borne vibrations propagate into the soil and can transmit through geological structures. The intensity of ground shaking depends at least on the physical properties of the source of vibrations, including its strength and frequency content, the soil mechanical properties, and the distance from the source. High-energy natural transient vibrations, such as earthquakes that may damage or even collapse structures (Viens et al., 2018), are under ongoing long-term monitoring to prevent natural hazards and to perform geophysical imaging of the Earth's interior. Artificial transient vibrations of high energy, such as blast loads including quarrying explosions and mining activities, may also cause structural damages (Kumar et al., 2016) and have thus lead to numerous recent works to predict blast-induced vibrations (Kumar et al., 2016; Li et al., 2019; Murmu et al., 2018; Nateghi, 2011). Lower energy transient signals of sledge hammer sources are commonly used in geophysical prospecting to image the subsurface at the decimeter scale (Ashida, 2001; Zhang et al., 2019). Steady-sate vibrations that result from continuous activities, such as pile-driving (Athanasopoulos & Pelekis, 2000), railway (Connolly et al., 2014; Nejati et al., 2012; With et al., 2006), and road traffic (Coquel & Fillol, 2017; Hao & Ang, 1998; Hunt, 1991; Meng et al., 2021) activities, are generally small in magnitude but act over long times: consequences may be discomfort and annoyance for the occupants of cars and residential homes rather than structural damage. However, damages may occur and modeling and experimental approaches (Crispino & D'apuzzo, 2001; Hao & Ang, 1998; Hunaidi & Tremblay, 1997; Hunt, 1991; Lak et al., 2011) have been developed to predict ground-borne vibrations that transit to buildings, bridges or tunnels located in close proximity to traffic roads.

Traffic-induced vibrations are generated by complex mechanical interactions between a moving vehicle and the road. The dynamic load on the irregular unevenness of the road surface generates stress waves, composed of surface and body seismic waves that propagate along the interface and into the soil with particular dominant frequency contents and amplitude motions (Barbosa, 2012; Gorges et al., 2019; Hao & Ang, 1998; Hunt, 1991). As a first approach, the amplitude decreases with the distance (Auersch & Said, 2010; Gutowski & Dym, 1976; Kim & Lee, 2000) but the seismic propagation may be complex, in particular inside tunnels (Abdel-Motaal et al., 2014; Clouteau et al., 2005; Fabozzi & Bilotta, 2016) which have motived studies on underground traffic (Chatterjee et al., 2003; Degrande et al., 2006; Fabozzi et al., 2017). Recently, Brenguier et al. (2019) have shown the potential of train traffic to monitor active faults using dense seismic arrays. In the present study, we consider an underground road traffic activity as a potential source of low-frequency mechanical vibrations which can be useful to detect and monitor large-scale structures around a motorway tunnel.

In Section 2, we present the geological context and the experimental setup of ground-borne vibrations measurements performed during one year in the research Underground Rock Laboratory (URL) of the Mont Terri (Switzerland), in the close vicinity of a motorway tunnel. Vibrations are recorded by geophones, introduced by quantitative comparison with a broad-band seismometer on an earthquake event. Section 3 deals with the identification and characterization of single traffic-induced events: we describe the data set, both in the time and frequency domains, and quantify the traffic-induced ground vibrations. We use a dynamic cross-correlation analysis to align the coherent traffic-induced traces. In Section 4, we analyze the root mean square (rms) of the wave traces and identify two particular features associated with different time-frequency responses. In Section 5, we develop the methodology to estimate the vehicle speeds and assess the seismic velocity of the rock mass to convert the recording time to the along-track position of the source along the motorway tunnel. In this spatial representation, we model the rms in order to identify both the material of the rock mass and the type of the source of vibrations associated with traffic-induced events. In Section 6, we quantify a contrast of attenuation properties that defines a bimaterial interface and highlight the type of dominant traffic-induced seismic waves based on a particle motion analysis. We finally discuss the origin of the seismically detected features surrounding the Mont Terri Main Fault.

2. Description of the Seismic Experimental Setup

2.1. The Mont Terri Experimental Site

The experiments presented in this work have been performed in 2015 in the Mont Terri URL (Bossart et al., 2018). The URL is located mainly in the Opalinus Clay of the Mont Terri (Figure 1a), with an overburden of about 300 m and along the longest tunnel of the A16 Transjurane motorway that crosses the Canton of Jura to link the Swiss plateau to France (Boidy et al., 2002). The Main Fault is the most prominent tectonic feature of the URL (Figure 1b, red zone): it is located at the center of the laboratory and characterized by a shear movement toward NNW (Jaeggi et al., 2018).

The motorway tunnel is a two-lane tube, 4,068 m in length and 7 m in diameter, for traffic in both directions with an NW-SE orientation. A security gallery, parallel to the motorway tunnel, gives access to the URL which is located at 2,800 m and 1,200 m from the NW and SE entrances of the tunnel, respectively (Figure 1a). In addition to traffic noise induced by moving vehicles inside the motorway tunnel, the URL is subject to many other mechanical sources of ground-borne vibrations, including borehole drilling operations, human activities, and ventilation systems for both the URL and the motorway tunnel. The mechanical sources are not constant in time and are associated with non-stationary noise sources characterized by frequency contents and statistical properties that may change over time. For identification purposes, long-term recording of the ambient vibrations is required in order to assess their identification (Peterson, 1993).

2.2. Ground-Borne Vibration Recording

The ground-borne vibration measurements have been performed in the gallery Ga08 of the Mont Terri URL, at an across-track distance $L = 95$ m from the motorway (Figure 1b). Vertical geophones (RTC-4.5Hz-395 by R.T. Clark Geophysical equipment) directly fixed to the clay rock at the bottom of vertical boreholes were

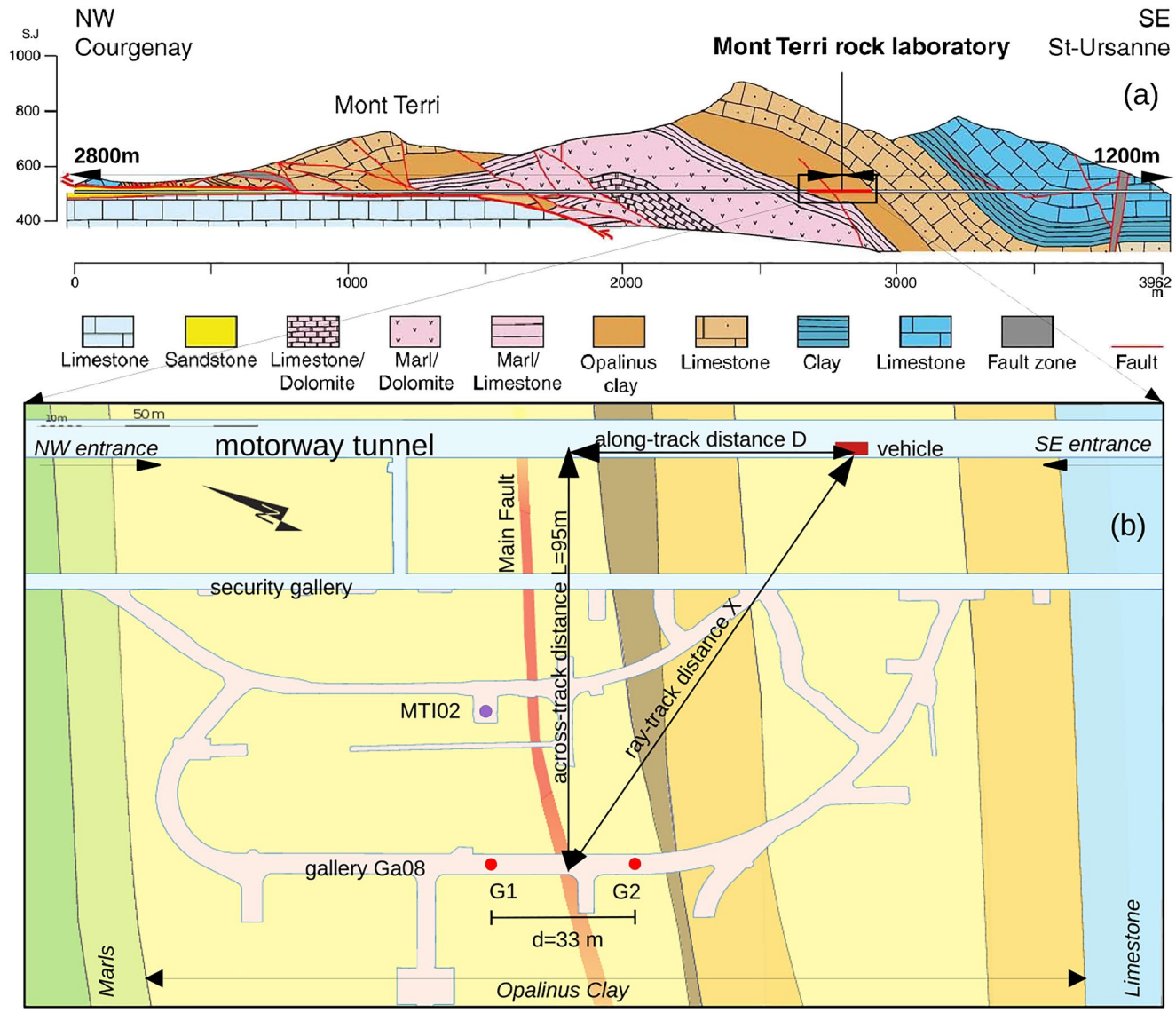

Figure 1. (a) The A16 Transjurane motorway tunnel crosses the Mont Terri: the Underground Rock Laboratory (URL, red segment) is mainly built in the Opalinus Clay (geological cross-section by Swisstopo). (b) The induced ground-borne vibrations are recorded by the use of two neighboring geophones (G1 and G2) in the gallery Ga08 of the URL.

used to measure the ground vibration velocity. The distance between the geophones is $d = 33$ m with an NW-SE orientation parallel to the motorway.

The geophones are connected to a Daqlink III, which is a 24-bit seismic data acquisition module, with a single seismic streamer unrolled in a groove drilled in the invert concrete. The acquisition of the signals is synchronous and controlled by a computer with the Vscope software. The geophones deliver a tension signal proportional to the vertical component of the ground velocity. They are characterized by a natural frequency $f_0 = 4.5$ Hz, a nominal sensitivity $S_0 = 23.4$ V/m/s, and a damping factor $\lambda = 0.7$: the sensitivity $S = S_0|HH^*|$ decreases at low frequencies according to the geophone frequency response $H = f^2 / \left(f_0^2 + 2i\lambda f f_0 - f^2\right)$.

The data files are continuous recording files of the ambient ground-borne vibrations sampled at 125 Hz and the duration of each file is 1 h. The data, acquired with the Daqlink format, are temporary stored in an internal memory Compact Flash card and sent through an Ethernet connection to the computer where

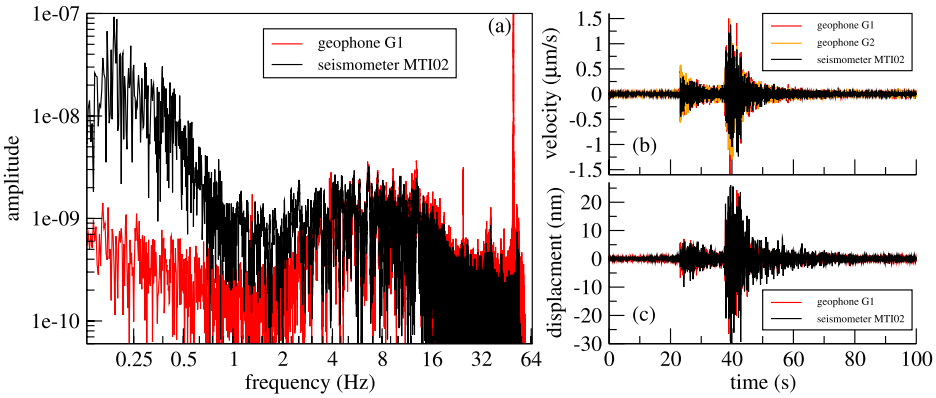

Figure 2. Earthquake event recorded by both the geophone G1 (red curves) and the vertical component of the MTI02 seismometer (black curves), (a) displayed in the frequency domain, (b) expressed in terms of velocity, and (c) displacement of the ground motion. The waveforms have been band-pass filtered in the frequency range of 3–48 Hz.

they are converted into Seismic Unix (SU) files of 400 s in duration for processing purposes (Cohen & Stockwell, 2017; Stockwell, 1999).

2.3. Quantification of the Ground Motion With an Earthquake Event

The RTC geophones are standard seismic receivers and a preliminary study consisted in checking the sensitivity and frequency response of the sensors, as well as the quality of the mechanical coupling with the clay rock. To do so, we consider the ground motion induced by a strong event simultaneously recorded and clearly identified by both an ordinary geophone and an STS-2.5 high-sensitive broadband triaxial seismometer. The STS-2.5 seismometer, located in the URL (Figure 1b, purple circle) and referred to MTI02 in the seismic data center of the Swiss Seismological Service, has a constant sensitivity for frequencies ranging between 0.01 and 50 Hz and is used here as a reference. The event is an earthquake of magnitude 2.2 that occurred on May 31, 2015, located at about 130 km from the Mont Terri.

The RTC geophone measurement highlights frequencies higher than 3 Hz when a constant sensitivity S_0 is considered (Figure 2a, red curve). The low-frequency content is not in agreement with the one captured by the MTI02 seismometer (Figure 2a, black curve) and is thus not considered. The geophone frequency spectrum is dominated by a peak at 50 Hz, which corresponds to electric noise that exists inside the URL where many experiments take place. In the following, the analysis is limited to the frequency band 3–48 Hz where it is in agreement with the frequency spectrum highlighted by the seismometer. By both band-filtering the signals in this frequency range and considering a constant sensitivity $S_0 = 23.4$ V/m/s for the geophone, the ground vibration velocity induced by the earthquake (Figure 2b) ranges between ± 1.5 μm/s and is associated to a vertical displacement in the range ± 25 nm (Figure 2c) in accordance to the seismometer measurements. Note the similarity between the waveforms recorded at the two geophones G1 and G2 (Figure 2b, red and orange curves, respectively). As a result, the RTC geophone velocity data are processed according to this quantitative approach.

3. Seismic Wave Signatures of Underground Traffic-Induced Events

3.1. Data Set Focused on Road Traffic Activity

The present study deals with ambient vibrations recorded in the Mont Terri URL by the geophones G1 and G2 (Figure 1b) from January to December 2015. Even if the data acquisition was interrupted many times during the experiment, the ground-borne vibration data set covers more than 88% of this period of time. The data set is structured into 70,000 SU traces. For each trace, a proxy used to quantify the energy of the ground-borne vibration is determined by integrating the frequency spectrum of the wave traces. This allows highlighting the temporal variations of the ground-borne vibration level as a function of the day of the year (Figure 3a) and the hour of the day (Figure 3b).

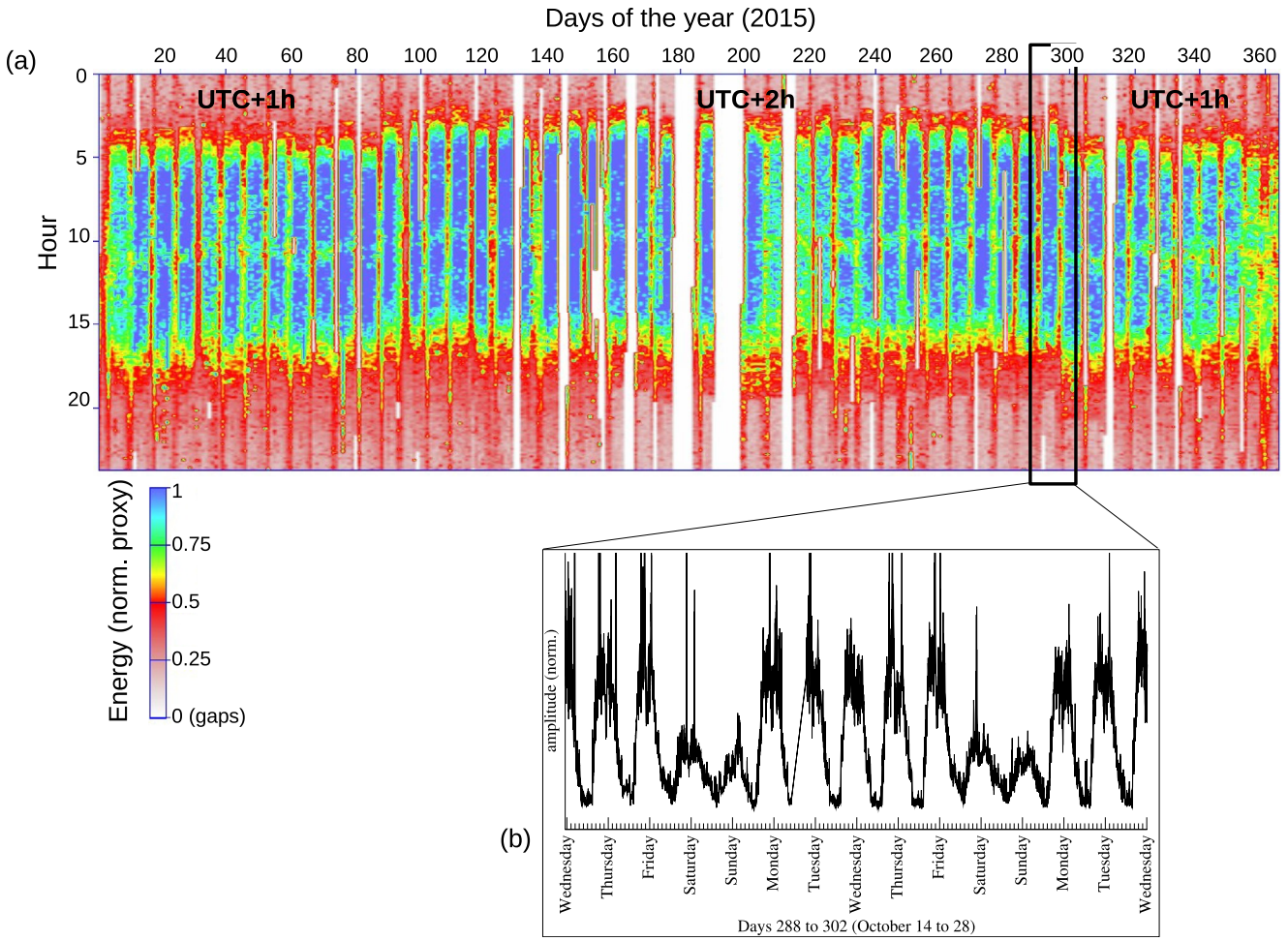

Figure 3. Temporal variations (UTC time) of the proxy energy of the ground-borne vibrations measured in the frequency range 3–48 Hz: (a) during the whole year 2015 (gaps in the data set are displayed in white color) and (b) a zoom in on a 2 weeks period of time.

As a first observation, dominant vibrations of the ground start at 5 a.m. and end at 9 p.m., with a minimum level at 1 p.m. which corresponds to a lunch break period: the intensity of the vibrations are lower during the weekends, in particular on Sunday nights, where anthropogenic sources of vibrations including human activities in the URL and traffic in the motorway tunnel are lower than during the week (Figure 3b). We thus focus on data recorded on Sundays between midnight and 4 a.m. when traffic activity consists of individual sources of ground-borne vibrations rather than continuous ambient noise. This approach allows statistical analyses of the URL ground response to mechanical vibrations induced by moving sources that go beyond the scale of the URL. The aim is now identifying traffic-induced signals and defining characteristic attributes to perform an automatic detection based on a sub-data set composed of 1,530 wave traces.

3.2. Traffic-Induced Ground Velocity

Successive traces recorded on day 50 by the geophone G2 illustrate the ground velocity measured inside the URL (Figure 4a). Each trace is characterized by a peak particle velocity PPV defined as the maximum instantaneous ground velocity during a given time window and commonly used as a site shaking intensity when dealing with the effect of vibrations on structures (Avellan et al., 2017; Connolly et al., 2014; Murmu et al., 2018).

Most of the traces are noise (Figure 4a, black traces), associated with low PPV values, and other (red traces) highlight strong events characterized by much larger PPV values (Figure 4b, black and red dots, respectively). The strong events, which do not appear regularly, are associated with waveforms characteristic of

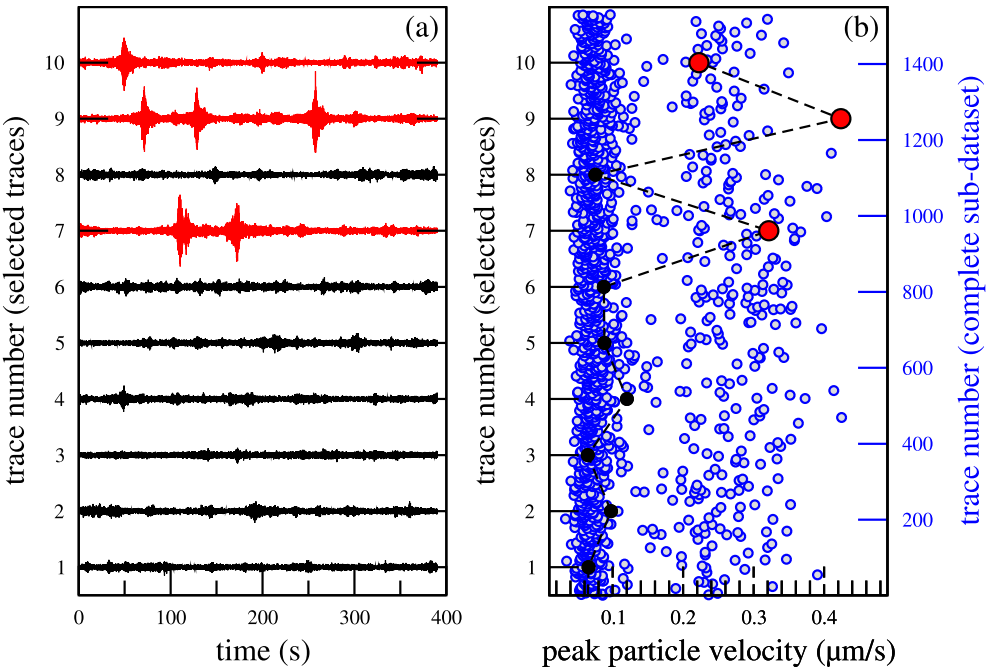

Figure 4. (a) Successive wave traces recorded on day 50 and (b) associated peak particle velocities (PPV): traffic-induced events (red dots), ambient noise (black dots), and PPV for the complete sub-data set (1,530 blue circles).

traffic-induced vibration signals (Hunaidi & Tremblay, 1997), that is they might be induced by individual moving vehicles driving through the motorway tunnel. When we extend this PPV analysis to the whole sub-data set (Figure 4b, blue dots), we put in evidence two main components of the noise level distribution characterized as a first approximation by normal distributions of different means and standard deviations (Figure 5a).

The first component (I) has a sharp (standard deviation $\sigma_I = 0.0004$) and high amplitude ($A_I = 12\%$) distribution centered on a low mean PPV value $\nu_I = 0.071\ \mu m\ /\ s$: it is associated to continuous ambient vibrations, induced for instance by ventilation systems and compressor engines. The second component (II) is characterized by a wide ($\sigma_{II} = 0.0040$) and low amplitude ($A_{II} = 0.75\%$) distribution centered on $\nu_{II} = 0.260$

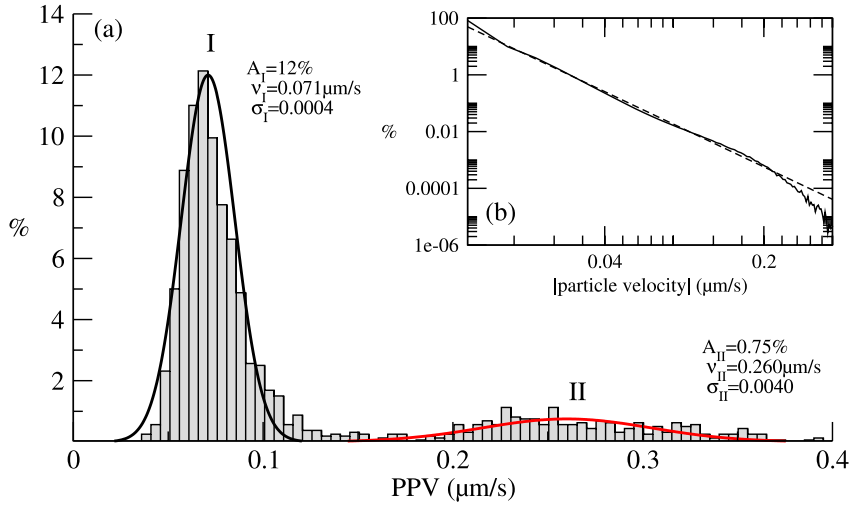

Figure 5. (a) Distribution of the peak particle velocities of the sub-data set (1,530 samples) recorded in the Mont Terri Underground Rock Laboratory on Sundays between midnight and 4 a.m. (b) Distribution of the absolute particle velocities (solid line, maximum value about 82%) and power law approximation (dashed line).

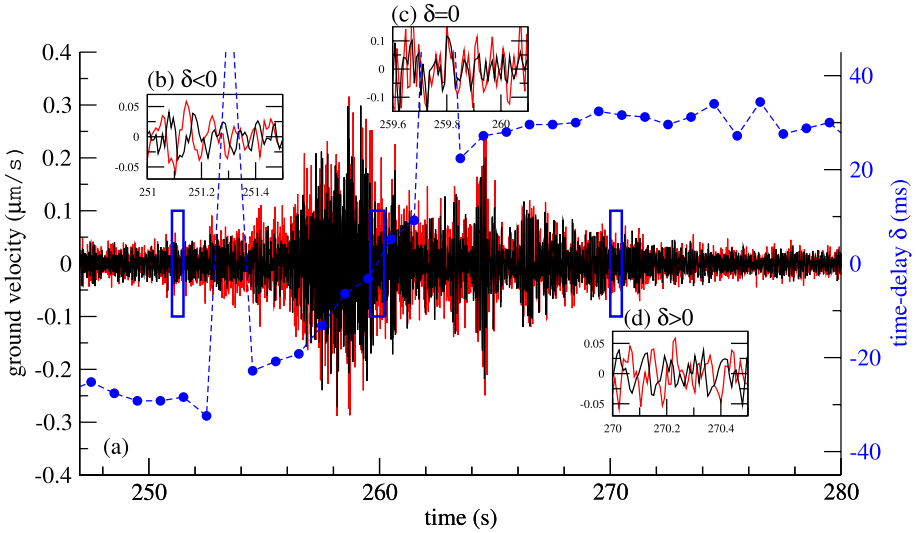

Figure 6. (a) Ground vibration traces of a traffic-induced event recorded simultaneously by geophones G1 (red curve) and G2 (black curve): the time-delay δ (blue dots) is (b) first negative, (c) then null, and (d) finally positive for a vehicle driving in the NW-SE direction.

μm / s: associated to traffic-induced events, less than 20% of the recorded traces belongs to this component. This suggests that the two main different sources of ambient vibrations, that is, low level continuous ambient noise and high level sharp traffic-induced events, might be identified based on a PPV threshold of 0.15 μm / s. Note that A_I and A_{II}, measured for 400 s seismic traces, depend on the window length. Interestingly, the absolute particle velocities continuously measured in the sub-data set (Figure 5b) follows a power law up to velocities about 0.2 μm / s which nearly corresponds to the PPV threshold quantified for traffic-induced events.

The ground motion is induced by complex mechanical interactions between the vehicle and the soil, including static load related to the vehicle weight and dynamic load that depends on the vehicle speed, the soil type, structure, and irregularities (Crispino & D'apuzzo, 2001; Kim & Lee, 2000; Lak et al., 2011; Watts & Krylov, 2000). These forces contribute to the oscillation of the vehicle that generates ground vibrations. Inside the Mont Terri motorway tunnel, the traffic speed is limited to 80 km/h but differences in both the speed and types of moving vehicles induce a wide range of ground velocities measured between 0.15 and 0.35 μm / s. Such values remain far below the damage and perceptible thresholds reported in the literature (Hunaidi & Tremblay, 1997; Nateghi, 2011), about few mm/s for underground structures like tunnels (Studer & Suesstrunk, 1981), because in the present experiment, the traffic-induced events are recorded at large distances and across many structures, including security and reconnaissance tunnels, galleries and niches and boreholes that make the wave propagation very complex.

3.3. Cross-Correlation of Traffic-Induced Waveforms

Based on the PPV threshold defined in the previous section, the traffic-induced events can be identified automatically in the data set and associated with individual vehicles that move in the motorway tunnel. However, we do not have any information on the temporal positions of the vehicles, such as the times they enter the tunnel. The aim is now to define a time reference to coherently align the traffic-induced wave traces.

The ground-borne vibrations are recorded simultaneously by two geophones (Figure 6a). For a vehicle entering the tunnel from the NW entrance, the local ground velocity increases when the vehicle gets close to the geophones and the trace detected at G1 is first in advance to the trace recorded at G2 with a time delay $\delta < 0$ (Figure 6b). At longer times, the two traces become similar with $\delta = 0$ (Figure 6c). After then, the wave trace detected at G2 is in advance to the wave trace recorded at G1 with a time delay $\delta > 0$ (Figure 6d). The time-delay δ corresponds to the time lag τ associated to the maximum value of the normalized cross-correlation function (Snieder, 2002; Stähler et al., 2011):

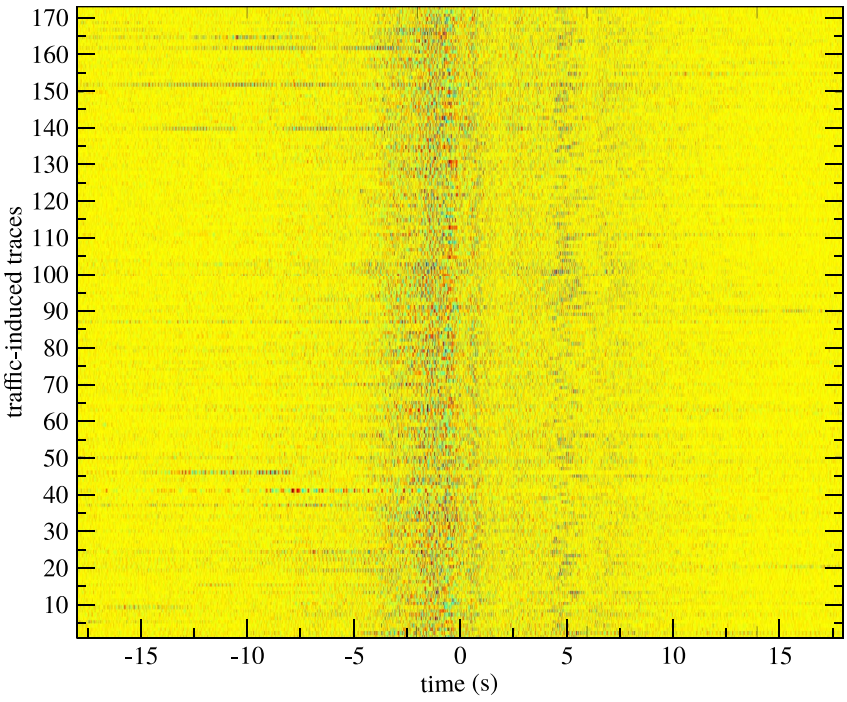

Figure 7. Traffic-induced wave traces (173 events, normalized amplitudes) recorded by the geophone G2, all re-oriented in the NW-SE driving direction inside the Mont Terri motorway tunnel. The traces are arbitrarily aligned at the reference time defined by $\delta = 0$.

$$C_{1,2}(\tau) = \frac{\int_a^b G_1(t)G_2^*(t-\tau)dt}{\sqrt{\int_a^b G_1(t)G_1^*(t-\tau)dt}\sqrt{\int_a^b G_2(t)G_2^*(t-\tau)dt}} \quad (1)$$

where $G_1(t)$ and $G_2(t)$ are the seismic traces recorded at G1 and G2, respectively, and the asterisk indicates the complex conjugate. The time-delay δ is determined with a sliding time window $b - a = 1$ s at successive recorded times (Figure 6a, blue dots). The small distance between G1 and G2 makes the recorded waveforms highly coherent: this is a condition for analyzing the traffic-induced data set. Note that the approach has similarities with the recent seismic stereometry method applied to earthquakes recorded at two neighboring seismic stations (Mordret et al., 2020).

The sign of the time-delay δ is an indicator of the driving direction of the vehicle inside the motorway tunnel: a negative (positive) time delay at the start of the traffic-induced event means a NW-SE (SE-NW) driving direction. In the following, we consider the time associated to $\delta = 0$ as the reference time and use it to align the traffic-induced seismic traces (Figure 7). Note that truncated events located at the start or end of the seismic trace, as well as multi traffic-events, are not considered. The data processing based on this approach highlights a good coherency between the traffic-induced events measured at different periods of time and all re-oriented to the NW-SE direction. Finally, the analysis deals with 173 ground vibration traces that can reliably be associated with single traffic-induced events entirely recorded in 36 s time windows.

3.4. Frequency Signature of the Traffic-Induced Ground Vibration

Taking advantage of the time shifted traffic-induced traces aligned on the reference time defined by $\delta = 0$, we are able to determine the mean frequency content focused on the traffic-induced events (Figure 8).

Electronic noises have been removed by band-reject filtering, including the 50 Hz sub-harmonic at 25 Hz and the 16.66 Hz of the train station located at the SE entrance of the Mont Terri tunnel. As a first approximation, the frequency content associated with traffic-induced events (Figure 8, bold curve) is characterized by two broad frequency bands. The first band covers the frequency range 30–40 Hz and can also be

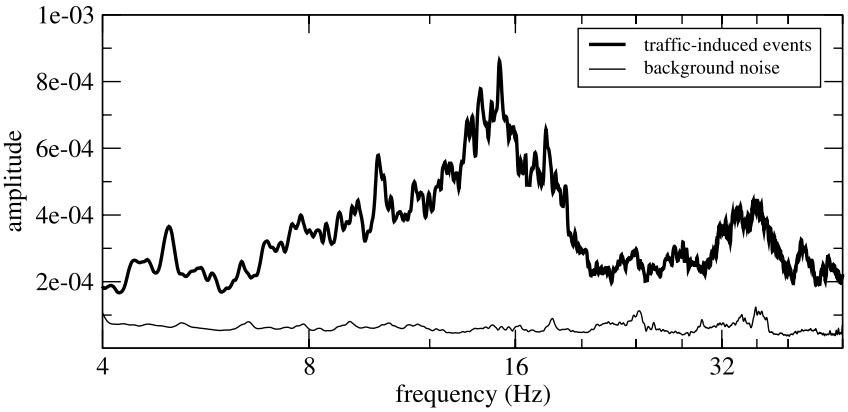

Figure 8. Mean frequency spectra associated with background noise (thin curve) and traffic-induced events (bold curve).

identified in the background noise (Figure 8, thin curve) associated with no traffic activity and characterized by a nearly flat spectrum. The second band covers the frequency range 10–20 Hz which is weak in the background noise and can thus be considered as the main frequency content that characterizes the traffic-induced events: several frequency peaks can be observed and may be attributed to galleries, boreholes, or niches that may be excited into resonance by ambient mechanical vibrations induced by traffic inside the motorway tunnel. As a first approach in large-scale seismic imaging the Mont Terri URL, the traffic-induced events may be used as extended sources of vibrations recorded at two geophones instead of a more rigorous ambient seismic noise imaging approach (Roux et al., 2005; Stehly et al., 2006) that would consist in considering a homogeneous distribution of sources recorded by a dense array of sensors.

4. Identification of Two Large-Scale Features From Root Mean Square Analysis

In their work, Lak et al. (2011) present ground-borne vibrations induced by the passage of a truck at a speed of 50 km/h and the associated running rms (with a time window of 1 s) profiles measured at different distances from the road. Not discussed by the authors, the rms profile measured at small distances (4 m) is nearly symmetric and becomes asymmetric when measured at larger distances (64 m): the vehicle speed (14 m/s) is much lower than the wave velocity in the soil (>150 m/s for depths larger than 50 cm), suggesting that the directivity effect of the excitation source may be neglected, and we assume that this asymmetry may be related to large-scale heterogeneities that may exist in the rock mass surrounding.

Similarly, we compute the 1 s running rms velocity $\sqrt{\sum_{i=1}^{n} \frac{v_i^2}{n}}$, where v_i is the instantaneous vertical ground-borne velocity measured in the Mont Terri URL at the across-track distance $L = 95$ m from the motorway and $n = 125$ (Figure 9, gray dots).

By averaging the results based on the geophone G2, a reliable average rms profile can be highlighted (Figure 9, black dots). At large times t, the rms tends to a constant as low as 0.007 μm/s. For t ranging in ±15 s, the rms profile is strongly asymmetric and composed of two peaks (A and B). The result is similar for the analysis based on the geophone G1, with a nearly constant amplitude ratio of about 1.2 (Figure 9, black circles). The primary peak (A), with a maximum rms amplitude about 0.06 μm/s, is measured at $t_A \simeq -1$ s. If the rock mass were isotropic and homogeneous, the maximum rms value measured at G2 should be located at $t > 0$: this highlights that the traffic-induced vibrations propagate through a heterogeneous rock mass. The secondary peak (B), with a maximum rms amplitude about 0.04 μm/s, is measured at the time $t_B \simeq 5$ s toward the SE entrance of the motorway tunnel. The position of the peak does not depend on the driving direction of the vehicles along the motorway tunnel: it is detected after the peak A for vehicles coming from the NW and before for the opposite driving direction. As a consequence, the peak B is associated to an unexpected local feature rather than a reflection of the feature A at the free surface of the Mont Terri for instance: features A and B may be generated by different sources of ground-borne vibrations. To go further into this

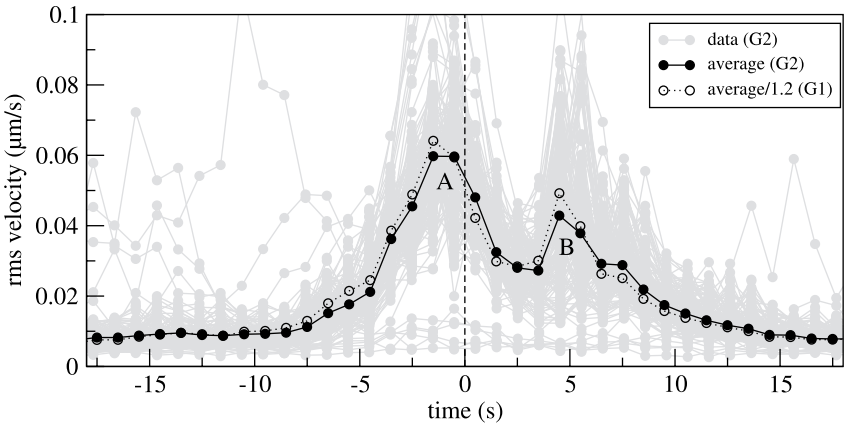

Figure 9. Root mean square (rms) profiles of traffic-induced wave traces recorded at G2 (gray dots) and average profile (black dots). The average rms profile measured at G1 is also shown (black circles).

analysis, we perform time-frequency analysis of the recorded traces based on a running Fourier transform with a time window of 1 s and an overlapping of 50% (Figure 10).

On average, the spectrogram clearly highlights differences in the frequency contents of the two features, that is, in the range 12–20 Hz with a dominant frequency of 15 Hz for A and in the range 9–12 Hz with a dominant frequency of 10 Hz for B.

5. Methodology to Locate and Characterize the Features Along the Motorway Tunnel

5.1. Seismic Location Based on Individual Vehicle Speeds and Seismic Velocity

In the present study, the reference time is arbitrary located at the time-delay $\delta = 0$. In order to spatially locate the two features A and B along the motorway tunnel, both the vehicle speed v and the seismic velocity V of the rock mass are required.

As introduced in Section 3.2, the spreading of the PPV values associated with traffic-induced events may be related to different types and speeds of the vehicles. Inside the motorway tunnel, the maximum authorized speed is $v_0 = 80$ km/h: actually, the real speeds associated with the measured traffic-induced events are unknown, with an average that should be about v_0. A first approach consists in taking advantage of the feature B which time detection t_B slightly differs from a traffic-induced event to another and can thus be used to assess differences in the moving speeds of the vehicles. For an average speed v_0 and an average time location of B about 5 s, the approximate spatial location is 110 m, a mean value used to estimate speed fluctuations.

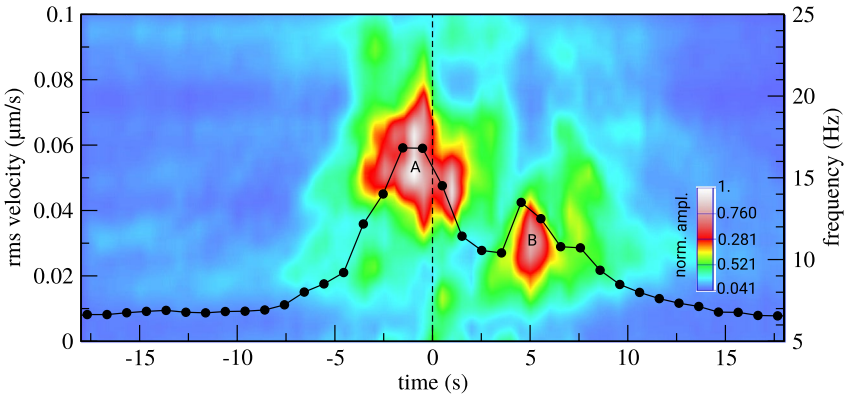

Figure 10. Average time-frequency representation of the traffic-induced events (normalized color scale): the two peaks of the root mean square velocity are associated with different seismic frequency contents.

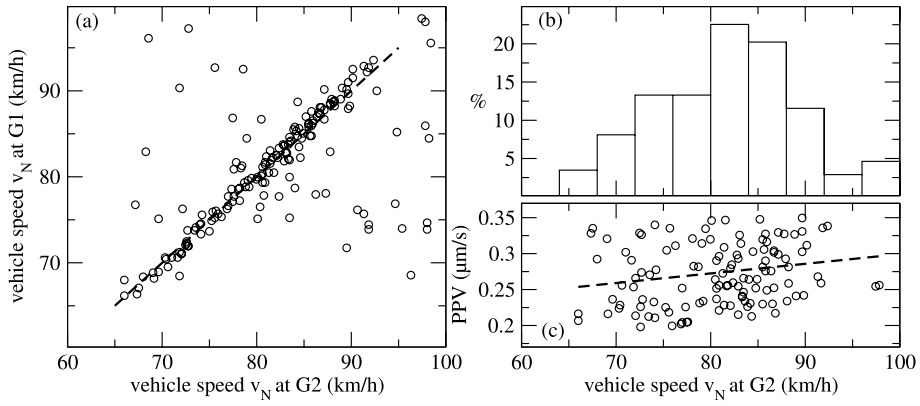

Figure 11. (a) Vehicle speeds v_N associated to the traffic-induced events estimated at the two geophones G1 and G2 from the time detection of the feature B (equality in dashed line). (b) Distribution of the vehicle speeds. (c) Peak particle velocity plotted as a function of the vehicle speed (linear fit in dashed line).

The approach is performed to all traffic-induced events, both at G1 and G2 (Figure 11a), and shows that about 80% of the individual vehicle speeds v_N spreads in the range 70–90 km/h (Figure 11b) with an average about 82 km/h. Note that an increase of the PPV with the vehicle speed is not obvious (Figure 11c) and may thus be more dependent on the vehicle type (weight, tires, suspensions, etc.) than on the speed which remains in a limited range.

In a second approach, we consider the time-delay $\delta(t)$ measured by cross-correlating the waveforms simultaneously recorded at G1 and G2 (see Section 3.3). At the recording time t, the time-delay can be modeled by $\overline{\delta}(t) = t_1 - t_2$ defined as the difference between the times $t_1 = \sqrt{\left(D(t) + d\,/\,2\right)^2 + L^2}\,/\,V$ and $t_2 = \sqrt{\left(D(t) - d\,/\,2\right)^2 + L^2}\,/\,V$ when the seismic wave arrives at G1 and G2, respectively, with a propagation inside the rock mass at the seismic velocity V. The along-track position $D(t)$ of the vehicle along the motorway tunnel can be determined according to recent works by Meng and Ben-Zion (2018) and Meng et al. (2021): when the vehicle generates a wave at the time t', the wave arrives at the geophone at the time $t = t' + \sqrt{\left(vt'\right)^2 + L^2}\,/\,V$. By considering that the vehicle speed v is much lower than the seismic velocity V, the time at the source is given by $t' = t - \sqrt{\left(vt\right)^2 + L^2}\,/\,V$ (Meng et al., 2021) and we can express the along-track position $D(t) = vt'(t)$ by the non-linear relationship:

$$D(t) = v\left(t - \frac{\sqrt{\left(vt\right)^2 + L^2}}{V}\right) \tag{2}$$

which gives a reference along-track position at $D(0) = -vL\,/\,V$. The velocity V is unknown but an order of magnitude can be estimated based on the traffic-induced event displayed in Figure 6: it is associated to a vehicle speed about 87 km/h, defined from the previous approach, and the time-delay measured at the time –10.5 s is –29.2 ms, which corresponds to a seismic velocity of 1,061 m/s and a reference position at –2 m. As a first approach, $D(t) \simeq vt$ allows modeling the time-delay by

$$\overline{\delta}(t) \simeq \frac{vt}{\sqrt{L^2 + (vt)^2}}\frac{d}{V} \tag{3}$$

based on the assumption $d \ll L$ or $d \ll D$, and assessing the vehicle speed according to the approximation

$$v(t) \simeq \frac{L}{|\,t\,|\sqrt{\dfrac{d^2}{V^2\overline{\delta}^2(t)} - 1}} \tag{4}$$

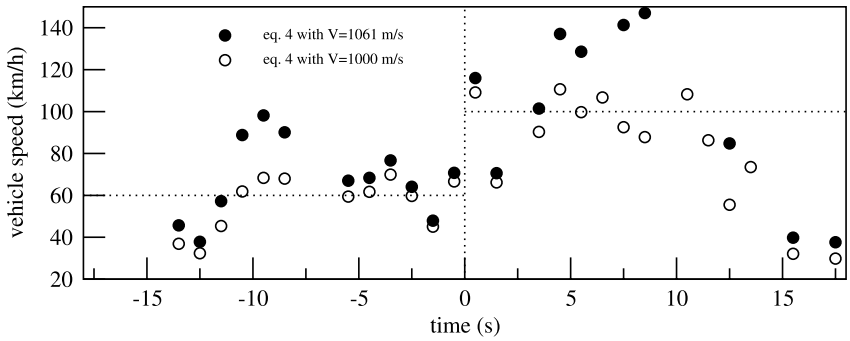

Figure 12. Inversion of the vehicle speed of the traffic-induced event is shown in Figure 6 (Equation 4).

that requires both $t \neq 0$ (equivalent to $\delta(t) \neq 0$ by definition in the present study) and $d > V\delta(t)$. We use this simple kinematic model to assess the vehicle speed as a function of the relative time t: it is about 60 km/h for negative times and 100 km/h for positive times where fluctuations with the velocity V = 1,061 or 1,000 m/s increase locally (Figure 12, black and empty disks, respectively). The motorway is on a straight line inside the Mont Terri and it is unlikely that the vehicle speed considerably increases after passing $t = 0$ for all the vehicles, suggesting a non-constant velocity V rather than abrupt changes of the moving speed v. Since v depends on the traffic-induced event, it is noted v_N.

As a consequence, we define the following process to convert the recording time t to the along-track position D of the vehicle along the motorway tunnel. In a first step, the time-delay is measured as a function of $t \times v_N \,/\, v_0$ for each traffic-induced event (Figure 13a, gray dots), where v_N and the mean speed v_0 are defined from the approach described above (see Figure 11). The measurements of δ are associated to correlation coefficients $C_{1,2}$ (see Equation 1) which show a maximum at the two peaks A and B for all events (Figure 13b), about 0.94 and 0.9, respectively, and can reach very low values outside these peaks. In the second step, data associated to both $C_{1,2} < 0.7$ and spurious time-delays are removed to define the average curves for δ and

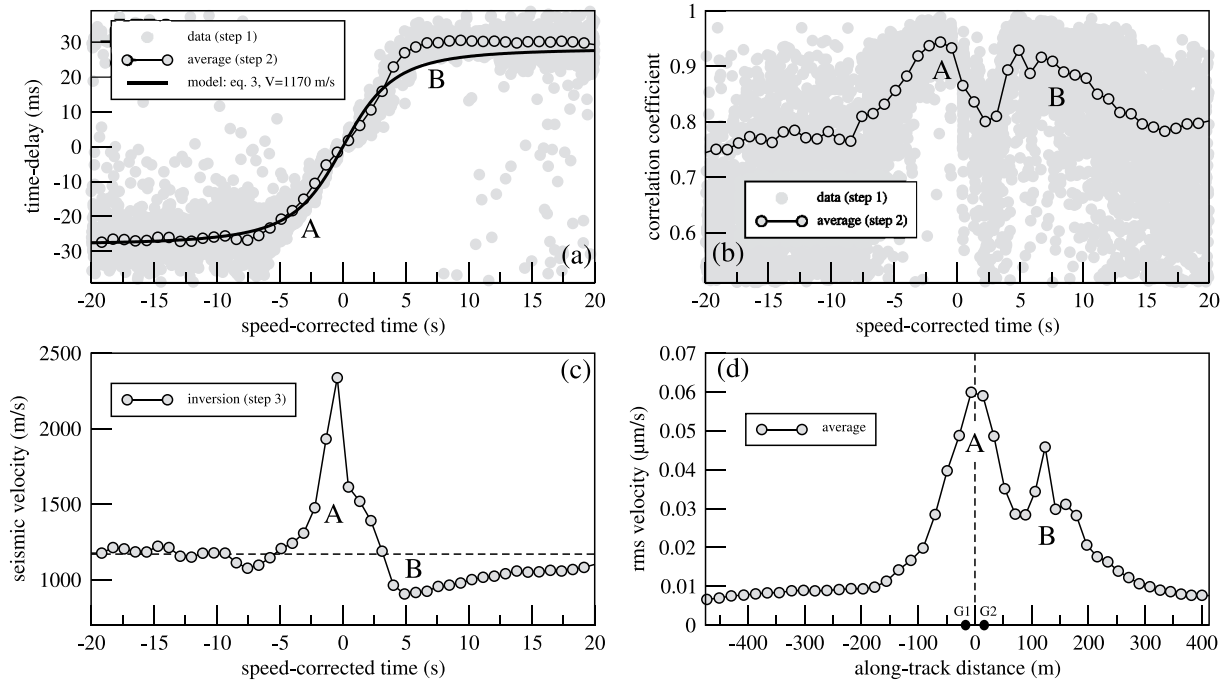

Figure 13. Data (gray dots) and average (circles) of (a) the time-delay associated with the model given by Equation 3 (solid line), (b) the normalized cross-correlation coefficient, and (c) seismic velocity of the rock mass, displayed as a function of the time corrected from the vehicle speed v. (d) Representation of the average rms curve (see Figure 9) as a function of the along-track distance which takes into account both v and V.

$C_{1,2}$ (Figures 13a and 13b, circles). In the third step, we determine the seismic velocity V of the medium as a function of the speed-corrected time t axis by optimizing the model $\overline{\delta} = t_1 - t_2$ associated to the general form of D (Equation 2) for a constant speed v_0 (Figure 13c): the seismic velocity ranges between 800 and 2,300 m/s. Note that V is lower than small-scale measurements commonly performed at ultrasonic frequencies in the Mont Terri URL: with a sounding wave at 30 kHz, which can propagate only few meters inside the rock mass, the velocity is larger than 2,700 m/s (Le Gonidec et al., 2014), that is, a source of few Hz may lead to different velocities because of the complex structure of the rock mass (galleries, boreholes, niches, etc.). The asymmetry of the seismic velocity relative to $\delta = 0$ explains the time-shift at negative times of the maximum amplitude of both the correlation coefficient and the rms velocity.

In the last step, the along-track position D is finally determined according to Equation 2 and used to display the measurements with respect to the position of the vehicle along the tunnel. According to the similarity between the rms profiles for the geophones G1 and G2 (see Figure 9), it is likely that the maximum amplitude of the average profile associated with the peak A is located between G1 and G2: we arbitrary consider the reference along-track position $D_A = 0$. As a result of the processing steps described above, the rms velocity displayed as a function of t (Figure 9) is not similar to the rms velocity displayed as a function of D where the peak A is nearly symmetric relative to $D_A = 0$ and the peak B is located at about 130 m and characterized by a complex fine-scale structure (Figure 13d).

5.2. Modeling the Root Mean Square to Quantify Geometric and Intrinsic Damping Coefficients

In the previous section, the two features A and B identified from the rms velocity have been located along the motorway tunnel: this allows studying the amplitude of the traffic-induced vibrations measured by the geophones as a function of the along-track position of the source. To that aim, we define a model in order to describe the data in terms of seismic attenuation properties. As a first approximation, we consider that the instantaneous velocity v_i can be written as the sum of three main contributions associated to the features A (v_i^A) and B (v_i^B) and to the background ambient vibrations C (v_i^C) induced by continuous nearby experiments inside the URL. The model of the global rms is thus:

$$\overline{rms} = \sqrt{\sum_{i=1}^{n} \frac{\left(v_i^A + v_i^B + v_i^C\right)^2}{n}} = \sqrt{\sum_{i=1}^{n} \frac{(v_i^A)^2 + (v_i^B)^2 + (v_i^C)^2 + \dots}{n}} \tag{5}$$

which is approximated by:

$$\overline{rms} \simeq \sqrt{\mathrm{rms}_A^2 + \mathrm{rms}_B^2 + \mathrm{rms}_C^2 + \mathrm{rms}_{\mathrm{noise}}^2} \tag{6}$$

where rms_{noise} is the noise level about 0.007 μm / s that does not depend on the along-track position.

According to recent blasting (Avellan et al., 2017; Kumar et al., 2016; Nateghi, 2011), pile-driving (Athanasopoulos & Pelekis, 2000) or other technical sources including the railway and road traffics (Auersch & Said, 2010; Gutowski & Dym, 1976; Yu et al., 2021), a power law is commonly used to model the ground vibration decay with the distance. The model is defined by the Bornitz's equation (Kim & Lee, 2000; Taniguchi & Sawada, 1979; Yang, 1995), used here to model the rms velocity:

$$\mathrm{rms}_A = \mathrm{rms}_A^0 \left(\frac{X_A^0}{X_A}\right)^{n_A} e^{-\alpha_A\left(X_A - X_A^0\right)} \tag{7}$$

where the across-track distances $X_A^0 = \sqrt{D_A^2 + L^2}$ and $X_A = \sqrt{(D_A - D)^2 + L^2}$ locates the maximum value at the along-track position D_A, rms_A^0 is the rms value at $D = 0$. The parameter n_A is the attenuation radiation damping coefficient of the seismic wave and α_A the intrinsic damping coefficient that characterizes the surrounding rock mass material. Equivalent notations are used for the two other components B and C.

The problem is composed of 13 parameters (4 for each component A, B and C, and the noise) and is solved numerically by a simulated annealing inverse procedure that takes into account the four contributions simultaneously. The reference position is fixed to $D_A = 0$. The location of the feature B has been estimated from the rms analysis about 130 m but we search for its position D_B in the broad range 110–160 m. The maximum amplitude of the component rms_C induced by nearby experiments is expected to be located in

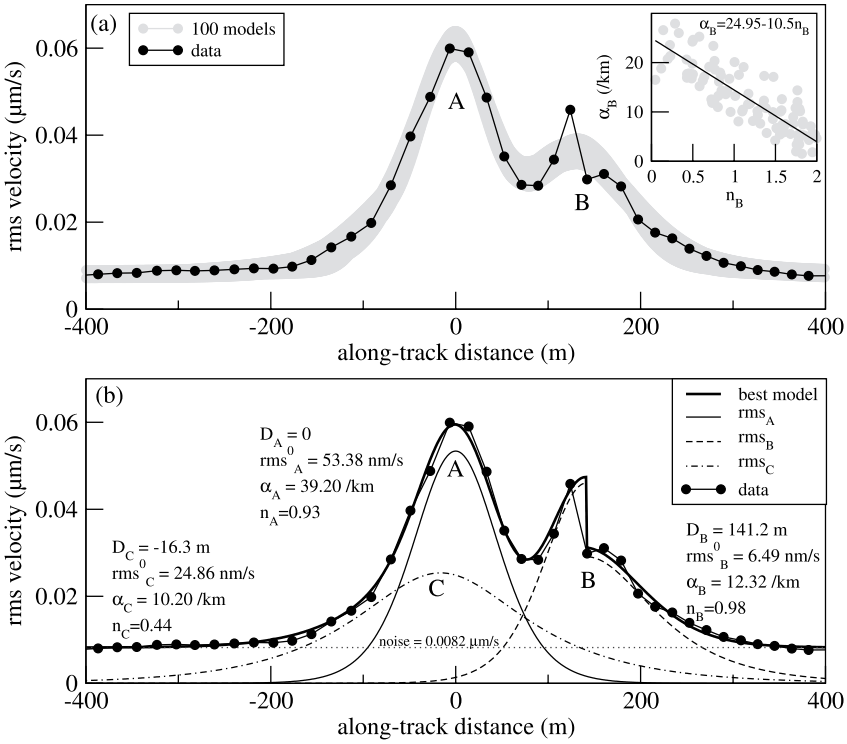

Figure 14. (a) One hundred models based on optimized parameter ranges (gray dots): the trade-off effects of n_B and α_B compensate (linear relationship) when fitting the data (black dots). (b) Best root mean square model (solid bold curve and parameters) and models of the features A and B and background vibrations C inside the Underground Rock Laboratory for 12 free parameters and B splitted into the A material for $D < D_B$ and the B material for $D \geq D_B$.

the URL, that is, at an along-track position within ±100 m. The rms^0 parameter for the three components is searched in the range 0–0.06μm/s, limited to the maximum amplitude of the rms data. The α parameter for the three components is searched in the range 0–70/km, the upper boundary being larger than material damping coefficients published in the literature (Athanasopoulos & Pelekis, 2000; Madshus & Kaynia, 2000; Takemiya, 2003). The parameter n ranges in 0–2, which boundaries correspond to no attenuation of surface waves and a decrease as $1 / X^2$ for body waves generated by a point source located on the ground, respectively (Gutowski & Dym, 1976).

The inverse procedure highlights that some parameter ranges are over-estimated. For instance, D_B is mainly searched in 117–140 m and α_A and α_B in 25–65 and 2–30/km, respectively, but n_A and n_B remain in the whole range 0–2: one hundred models close to the rms data highlight the range of solutions for the global rms (Figure 14a, gray dots).

Perturbations of n_A have weak effects on rms$_A$, because A is located close to 0, but perturbations of n_B or α_B strongly modify rms_B located at a large distance: when fitting the global rms velocities, the trade-off effects compensate, according to an approximated linear relationship between n_B and α_B (Figure 14a, inset). The modeling can explain most of the rms data, but no solution has been found to fit the data located close to the center of the feature B which fine-scale structure is complex as highlighted by its high amplitude peak about 124 m. This is analyzed in details in the following section.

6. Bimaterial Interface and Dominant Polarized Body Waves

6.1. Discontinuity of the rms at the Bimaterial Interface Located at B

The model described in Section 5.2 shows that solutions in quantifying the physical parameters of the problem can be found for the whole feature A but only for the most distant part of the feature B which fine-scale structure is complex (Figure 14a). Actually, the center of B is located close to the transition between

Opalinus Clay and Limestone (Figure 1b): the model, based on homogeneous rock masses, has to be modified according to the local geology. We split rms_B into two parts, associated to the same geometric damping coefficient n_B but one in the Opalinus Clay with the intrinsic damping coefficient α_A and one in the Limestones with α_B, a transition located at the along-track position D_B searched in the range 110–160 m. As a result, the best model of the inverse procedure is in very good agreement with the whole data set, even at the center of the feature B (Figure 14b, bold curve) which complex structure can now be explained by the model as a sharp discontinuity of rock materials from $\alpha_A = 39.2$/km to $\alpha_B = 12.32$/km. This strong contrast of elastic properties defines a so-called bimaterial interface (Allam et al., 2014) located at the position $D_B = 141.2$ m. The features A and B are associated to different dominant seismic frequencies, about 15 and 10 Hz, respectively, suggesting a frequency-dependent response of the material (Aki & Chouet, 1975): as a first approximation, the material can be characterized by a frequency-independent attenuation coefficient α^0 by dividing the intrinsic damping coefficient α by the exciting frequency of the source of vibrations (Yang, 1995).

For the feature A, the geometric damping coefficient is $n_A = 0.93$: the coefficient is very close to 1 and means that a vehicle moving inside the tunnel is equivalent to an in-depth point source that generates body waves (Athanasopoulos & Pelekis, 2000), as expected in tunnel environments. The frequency-independent attenuation is $\alpha_A^0 = 2.61$ s/km, larger than the maximum values commonly measured from low-velocity surface wave measurements (Yang, 1995). Surface waves are less attenuated than body waves which may be associated with higher attenuation coefficients but very few studies are available for body waves: recently, Ren et al. (2019) have quantified attenuation in clays at about 10 m depth, lower for P-waves (0.1–0.11 s/km) than for S-waves (0.93–1.68 s/km). The present work deals with unusual underground experiments performed in the Opalinus Clay 300 m below the surface and the close vicinity of the heterogeneous structure of the Mont Terri URL, that is, α_A^0 is an effective parameter (Opalinus Clay and URL).

For the feature B, the geometric damping coefficient $n_B = 0.98$ is also very close to 1 in agreement with dominant body waves in the tunnel surrounding. The frequency-independent attenuation $\alpha_B^0 = 1.23$ s/km is in good agreement with near-surface silty clay materials measured with S-waves (Ren et al., 2019). The low seismic velocity V in the rock mass surrounding B is about 800 m/s, that estimates a quality factor $Q = \pi / \alpha_0 V$ about 4: it may correspond to the S-wave velocity but the wave propagates through an heterogeneous and anisotropic medium, that is, V is considered as a proxy velocity at this stage. For a better knowledge of the dominant waves that propagate from the source inside the motorway tunnel to the geophone inside the gallery Ga08, a particle motion analysis is performed on a traffic-induced event in the following section.

Note that the model also characterizes the background component C induced by continuous vibrations inside the Mont Terri URL (Figure 14b, dotted-dashed curve): with $n_C \simeq 0.5$, it is associated to surface waves generated by a point source on the ground (Athanasopoulos & Pelekis, 2000) located about −16.3 m, which may correspond to the long-term full-scale experiment that is located close nearby to the NW, where most of the Mont Terri on-site activity was recorded in 2015. The attenuation coefficient $\alpha_C^0 \simeq 0.68$ s/km falls in the range 0.580–0.775 s/km identified with near-surface measurements on rocks mainly composed of sandstones (Yang, 1995).

6.2. Dominant Polarized Body Waves Above the Main Fault

A three-component seismic receiver is required for a particle motion analysis. We identified the seismic data acquired by the MTI02 seismometer (available from the Swiss Seismological Service, see Section 2.3) that correspond to a traffic-induced event recorded by G2 (Figure 6, black curve). The seismometer simultaneously records three waveforms in the North, East and vertical (vert.) directions but they are not synchronized with the geophone data set (Figure 15a, gray curve and dots). We simultaneously shift the seismometer waveforms (Figure 15a, black curves) in order to align the rms of the vertical component with the averaged rms measured at G2. The particle motion analysis is not straightforward because of the source, and as a consequence, the plane of propagation is continuously changing. Thus, we consider broad time windows to display the particle motion in the longitudinal-transversal and longitudinal-vertical planes (the transversal axis is perpendicular to the longitudinal axis which is oriented from the source to the receiver): 5 s

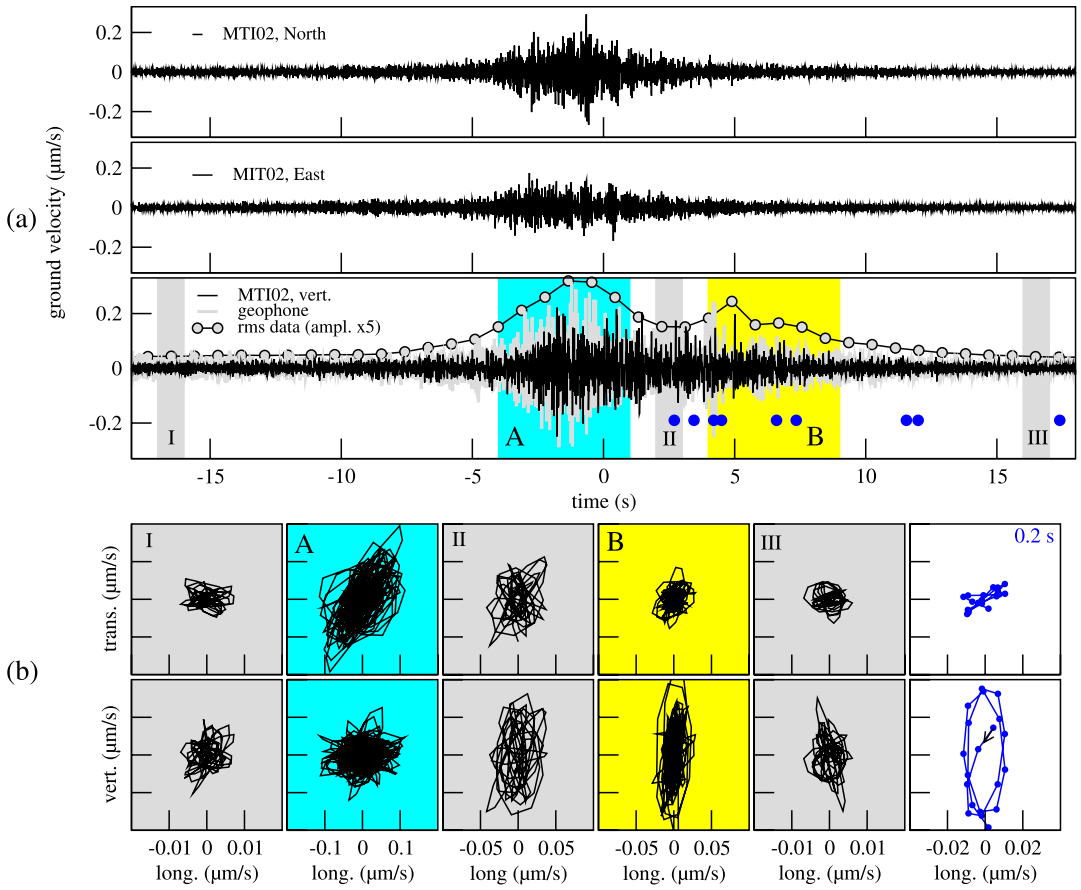

Figure 15. (a) Waveforms of a traffic-induced event were recorded by the three-component MTI02 seismometer (black curves) and the geophone G2 (see Figure 6). Factor 5 has been applied to the amplitude of the average root mean square profile (gray dots). (b) Particle motion was measured in different time windows (color) in the longitudinal-transversal (top) and longitudinal-vertical (bottom) planes. The measured in blue correspond to the identification of nearly pure Rayleigh waves characterized by a retrograde and elliptical behavior mainly confined in the longitudinal-vertical plane.

windows centered on the features *A* and *B* (Figure 15a, cyan and yellow zones, respectively) and 1 s windows located at (I) the beginning and (III) end of the event and (II) between *A* and *B* (Figure 15a, gray zones). The result highlight different behaviors of the particle motion with the position of the time window (Figure 15b).

An abrupt transition of the particle motion behavior is observed between the features *A* and *B*: the traffic-induced event vibrations are distributed along the three axes when t <0 and strongly focus in the longitudinal-vertical plane when t >0. At the main feature *A* (Figure 15b, cyan), dominant body waves propagate as a mixture of compressional (P), horizontally polarized shear (SH), and vertically polarized shear (SV) waves, with a proxy seismic velocity lower than the Opalinus Clay *P*-wave velocity. At the unexpected feature *B* (Figure 15b, yellow), seismic waves propagate mainly in the vertical plane: they can be SV waves and Rayleigh surface waves. Rayleigh waves propagate close and normal to the ground with retrograde and elliptical particle motion whose major axis is in the vertical plane: the analysis of the particle motion in 2 s windows detects a very small amount of such waves, limited to the positive recording times. At the feature *B*, SV waves dominate and the seismic velocity is mainly the SV-wave velocity measured at large scales.

As a consequence, the traffic-induced event is mainly associated with body waves, as expected in tunnel environments (Gutowski & Dym, 1976), and in agreement with the rms modeling approach used to assess the frequency-independent attenuation coefficient of the rock mass. Interestingly, the feature *A* is centered on the Main Fault which dips toward the SE, that is, a dominant mixture of body waves propagate deeper than the fault and dominant vertically polarized shear waves are recorded through the fault.

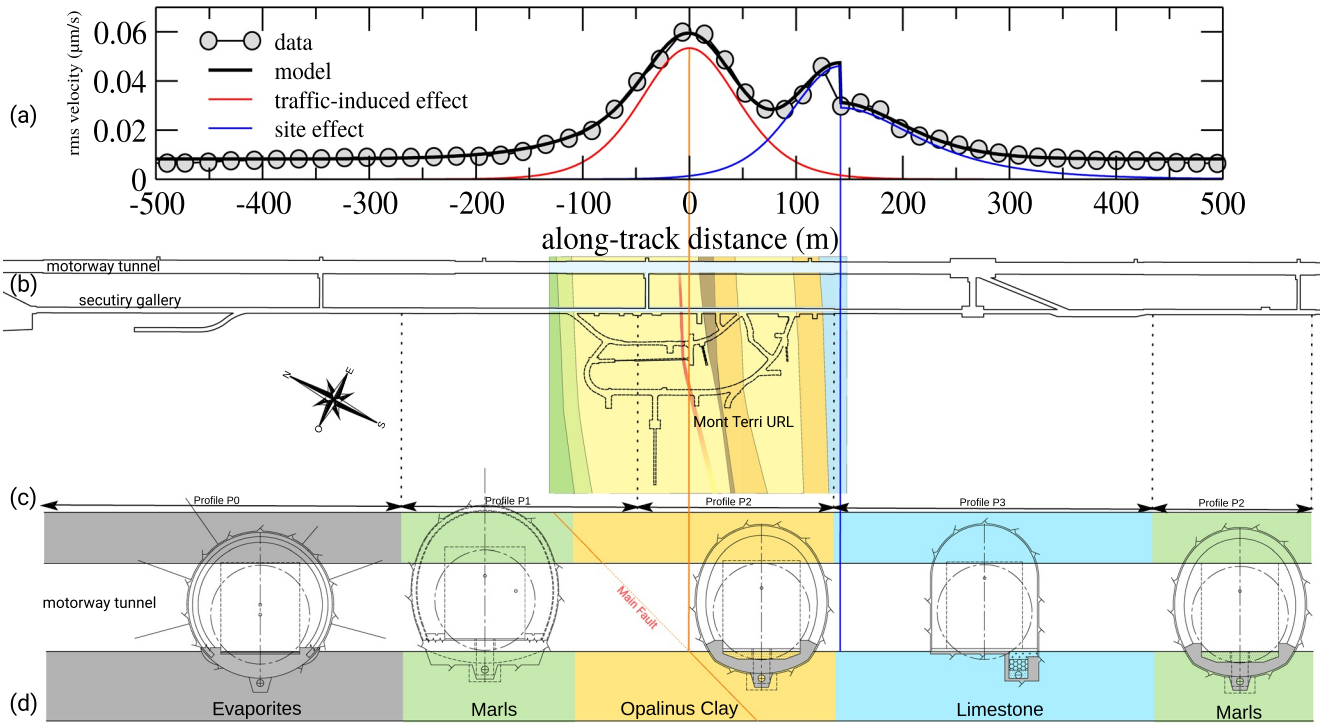

Figure 16. Correspondence between the locations of (a) the results based on the traffic-induced seismic recording of the present study (data and models of the root mean square velocity), (b) the tunnel and gallery network surrounding the Mont Terri Underground Rock Laboratory, (c) the local profiles of the motorway tunnel structure and (d) the simplified succession of rock materials.

6.3. Discussion on the Origin of the Unexpected Feature

The feature B detected from traffic-induced events in the Mont Terri URL is located at the along-track distance $D_B = 141.2$ m (Figure 16a). It is associated with both a local increase of the amplitude of the ground-borne vibrations and dominant vertically polarized shear waves. As a preliminary discussion, we identify the potential origins of this unexpected feature in the close vicinity of the Mont Terri URL.

The vehicles that generate the traffic-induced events move inside the motorway tunnel of the Mont Terri (Figure 16b): inside the tunnel, the wall is circular but the structure inside the rock mass is not the same all along the motorway (Figure 16c).

Most of the tunnel profiles have a nearly circular shape (profiles P0, P1, and P2) and only one has a horse-shoe shape (profile P3). As a consequence, the large-scale structure of the tunnel is characterized by two main discontinuities. The first discontinuity is located at the along-track distances 135 m, which is very close to the center of feature B (Figure 16c, vertical blue line) that could be generated by a local resonance inside the tunnel structure. But at the second discontinuity, located at the position 430 m, no feature has been detected in the seismic data set, may be because of attenuation or because the first discontinuity does not generate the feature B.

Actually, the tunnel profile is adapted to the rock material: in particular, its shape changes from circular (profile P2) to horseshoe (profile P3) between the Opalinus Clay and the Passwang Formation which contains Limestones. The transition Passwang Formation to Opalinus Clay is sharp and well-marked by a hard-ground indicating an erosional surface. Toward the South, close to the along-track position $D_B = 141.2$ m of the unexpected feature B, excavation has been performed in 2018 in the Passwang Formation: this allowed observing open fractures which disappear toward the North, including open solution enlarged fractures with cavities of up to 10 cm thickness and remaining fractures with an open space of less than 3 cm filled up with calcite. Such a heterogeneous fracture network can control the propagation of the seismic waves (Allam et al., 2014; Bulut et al., 2012) which may be trapped and guided (Ben-Zion & Sammis, 2003) to lo-

cally increase the ground-borne vibrations. Based on the rms modeling, the amplification factor measured at *B* is about 30, a high value that suggests an efficient local site effect controlled by the elastic properties of the rock mass (Cormier & Spudich, 1984; Yang & Sato, 2000).

The nearby Main Fault of the Mont Terri may act in a similar way on feature *A* but the effect is superimposed to the traffic-induced event itself. The dominant mixture of body waves that propagate below the Main Fault and the dominant shear waves that propagate at shallower depths may be related to different stress field conditions on either side of the Main Fault: this may both induce wave conversion processes (Levin & Park, 1997; Nakagawa et al., 2000; Ry et al., 2019) and contribute to the very high amplification of the ground-borne vibrations measured at the unexpected feature *B*.

7. Conclusions

One year of seismic recording in the Opalinus Clay of the Mont Terri URL located at 300 m depth has been performed by the use of two neighboring vertical geophones located 95 m away from the A16 Transjurane motorway in Switzerland. Based on ground-borne vibrations recorded between midnight and 4 a.m. on Sundays, we identified a data set of 173 traffic-induced events with peak particle velocities between 0.15 and 0.35 μm/s. By performing moving rms and time-delay analyses along the waveforms, we identified two particular features (*A* and *B*), associated with dominant frequencies about 15 and 10 Hz, respectively. Taking into account the vehicle speeds assessed from time shifts of the feature *B* relative to *A*, a simple kinematic model of the time-delay has been used to quantify the seismic velocity in the surrounding of the URL, from 1,170 to 2,300 m/s at *A* and down to 800 m/s at *B*. The approach has also been used to locate the features along the motorway tunnel, at the Main Fault for *A* and 141.2 m toward the SE entrance of the tunnel for *B*. A rms modeling based on the Bornitz's equation takes into account the spatial contributions of both *A* and *B*, generated by traffic-induced events, and the background vibrations generated by nearby experiments inside the URL. The model allowed quantifying (a) the geometric damping coefficient associated with dominant body waves as expected in tunnel environments, (b) the frequency-independent attenuation coefficients, about 2.61 s/km in the Opalinus Clay (including the URL) and 1.23 s/km for the Limestone, and (c) the location of the transition between Opalinus Clay and Limestones. The approach allows quantifying the coefficients for a nearly continuous and very large range of distances between the source and a single receiver, which is not available with common approaches. The particle motion analysis of a traffic-induced event recorded by the three-component MTI02 seismometer identified a mixture of body waves that propagates below the Main Fault and dominant vertically polarized shear waves recorded through the fault. We preliminary discussed the possible origins of the unexpected feature *B* in terms of (a) a bimaterial interface defined by the contrast of elastic properties between Opalinus Clay and Limestones, (b) trapped and guided waves in a heterogeneous fracture network, and (c) a site effect associated to an amplification factor about 30. Similar processes may occur at the Main Fault but are superimposed to the traffic-induced event itself.

The method, which requires the use of two neighboring standard geophones only, is promising for future works. In the surrounding of the feature *B*, karstic structures are formed from the dissolution of Limestone: during a rainfall activity, wet spots can be observed in the galleries, induced by an increase of pore-pressure inside the rock mass. It is of first interest to measure such temporal changes from a continuous recording of ambient body waves (Brenguier et al., 2020). The data set and methods presented in the present study can be used to that aim: traffic-induced events constitute reproducible, long-term, low-frequency, and non-destructive sources of vibrations well-suited to monitor rock mass properties at the scale of a gallery. A natural extension of the present work is thus long-term monitoring the response of the Mont Terri Main Fault to environmental changes.

Data Availability Statement

The ground-borne vibration data can be granted upon request to the Mont Terri Project Management.

Acknowledgments
This work belongs to the MO-A research project, supported by Swisstopo and the GNR FORPRO and performed in the Mont Terri URL. The authors thank the Swiss Seismological Service for providing access to waveform data recorded at the MTI02 seismometer located inside the Mont Terri and available for the research community from http://arclink.ethz.ch/webinterface. The authors would like to acknowledge the technical staff of Mont Terri URL, in particular, Thierry Theurillat and Senecio Schefer, and Fabrice Burrus from GGT SA (Delémont, Switzerland) for useful information on the Mont Terri tunnel. The authors also acknowledge an anonymous reviewer whose peer review contributed to improving the strength of the study.

References

Abdel-Motaal, M. A., El-Nahhas, F. M., & Khiry, A. T. (2014). Mutual seismic interaction between tunnels and the surrounding granular soil. *HBRC Journal*, *10*(3), 265–278. https://doi.org/10.1016/j.hbrcj.2013.12.006

Aki, K., & Chouet, B. (1975). Origin of coda waves: Source, attenuation, and scattering effects. *Journal of Geophysical Research*, *80*(23), 3322–3342. https://doi.org/10.1029/jb080i023p03322

Allam, A., Ben-Zion, Y., & Peng, Z. (2014). Seismic imaging of a bimaterial interface along the Hayward fault, CA, with fault zone head waves and direct P arrivals. *Pure and Applied Geophysics*, *171*(11), 2993–3011. https://doi.org/10.1007/s00024-014-0784-0

Ashida, Y. (2001). Seismic imaging ahead of a tunnel face with three-component geophones. *International Journal of Rock Mechanics and Mining Sciences*, *38*(6), 823–831. https://doi.org/10.1016/s1365-1609(01)00047-8

Athanasopoulos, G., & Pelekis, P. (2000). Ground vibrations from sheetpile driving in urban environment: Measurements, analysis and effects on buildings and occupants. *Soil Dynamics and Earthquake Engineering*, *19*(5), 371–387. https://doi.org/10.1016/s0267-7261(00)00008-7

Auersch, L., & Said, S. (2010). Attenuation of ground vibrations due to different technical sources. *Earthquake Engineering and Engineering Vibration*, *9*(3), 337–344. https://doi.org/10.1007/s11803-010-0018-0

Avellan, K., Belopotocanova, E., & Puurunen, M. (2017). Measuring, monitoring and prediction of vibration effects in rock masses in near-structure blasting. *Procedia Engineering*, *191*, 504–511. https://doi.org/10.1016/j.proeng.2017.05.210

Barbosa, R. S. (2012). Vehicle vibration response subjected to longwave measured pavement irregularity. *Journal of Mechanical Engineering and Automation*, *2*(2), 17–24. https://doi.org/10.5923/j.jmea.20120202.04

Ben-Zion, Y., & Sammis, C. G. (2003). Characterization of fault zones. *Pure and Applied Geophysics*, *160*(3), 677–715. https://doi.org/10.1007/pl00012554

Boidy, E., Bouvard, A., & Pellet, F. (2002). Back analysis of time-dependent behaviour of a test gallery in claystone. *Tunnelling and Underground Space Technology*, *17*(4), 415–424. https://doi.org/10.1016/s0886-7798(02)00066-4

Bossart, P., Bernier, F., Birkholzer, J., Bruggeman, C., Connolly, P., Dewonck, S., et al. (2018). Mont Terri rock laboratory, 20 years of research: Introduction, site characteristics and overview of experiments. In *Mont Terri Rock Laboratory, 20 years* (pp. 3–22). Springer. https://doi.org/10.1007/978-3-319-70458-6_1

Brenguier, F., Boué, P., Ben-Zion, Y., Vernon, F., Johnson, C., Mordret, A., et al. (2019). Train traffic as a powerful noise source for monitoring active faults with seismic interferometry. *Geophysical Research Letters*, *46*, 9529–9536. https://doi.org/10.1029/2019gl083438

Brenguier, F., Courbis, R., Mordret, A., Campman, X., Boué, P., Chmiel, M., et al. (2020). Noise-based ballistic wave passive seismic monitoring. Part 1: Body waves. *Geophysical Journal International*, *221*(1), 683–691. https://doi.org/10.1093/gji/ggz440

Bulut, F., Ben-Zion, Y., & Bohnhoff, M. (2012). Evidence for a bimaterial interface along the Mudurnu segment of the North Anatolian fault zone from polarization analysis of P waves. *Earth and Planetary Science Letters*, *327*, 17–22. https://doi.org/10.1016/j.epsl.2012.02.001

Chatterjee, P., Degrande, G., Jacobs, S., Charlier, J., Bouvet, P., & Brassenx, D. (2003). Experimental results of free field and structural vibrations due to underground railway traffic. *Citeseer*, 387–394.

Clouteau, D., Arnst, M., Al-Hussaini, T. M., & Degrande, G. (2005). Freefield vibrations due to dynamic loading on a tunnel embedded in a stratified medium. *Journal of Sound and Vibration*, *283*, 173–199. https://doi.org/10.1016/j.jsv.2004.04.010

Cohen, J., & Stockwell, J. (2017). *CWP/SU: Seismic Unix release 44: A free package for seismic research and processing*. Center for Wave Phenomena, Colorado School of Mines.

Connolly, D., Kouroussis, G., Giannopoulos, A., Verlinden, O., Woodward, P., & Forde, M. (2014). Assessment of railway vibrations using an efficient scoping model. *Soil Dynamics and Earthquake Engineering*, *58*, 37–47. https://doi.org/10.1016/j.soildyn.2013.12.003

Coquel, G., & Fillol, C. (2017). Analysis of ground-borne noise and vibration levels generated by buses. *Procedia Engineering*, *199*, 2699–2704. https://doi.org/10.1016/j.proeng.2017.09.564

Cormier, V., & Spudich, P. (1984). Amplification of ground motion and waveform complexity in fault zones: Examples from the San Andreas and Calaveras faults. *Geophysical Journal International*, *79*(1), 135–152. https://doi.org/10.1111/j.1365-246x.1984.tb02846.x

Crispino, M., & D'apuzzo, M. (2001). Measurement and prediction of traffic-induced vibrations in a heritage building. *Journal of Sound and Vibration*, *246*(2), 319–335. https://doi.org/10.1006/jsvi.2001.3648

Degrande, G., Schevenels, M., Chatterjee, P., Van de Velde, W., Hölscher, P., Hopman, V., & Dadkah, N. (2006). Vibrations due to a test train at variable speeds in a deep bored tunnel embedded in London clay. *Journal of Sound and Vibration*, *293*(3–5), 626–644. https://doi.org/10.1016/j.jsv.2005.08.039

Fabozzi, S., & Bilotta, E. (2016). Behaviour of a segmental tunnel lining under seismic actions. *Procedia Engineering*, *158*, 230–235. https://doi.org/10.1016/j.proeng.2016.08.434

Fabozzi, S., Licata, V., Autuori, S., Bilotta, E., Russo, G., & Silvestri, F. (2017). Prediction of the seismic behavior of an underground railway station and a tunnel in Napoli (Italy). *Underground Space*, *2*(2), 88–105. https://doi.org/10.1016/j.undsp.2017.03.005

Gorges, C., Öztürk, K., & Liebich, R. (2019). Impact detection using a machine learning approach and experimental road roughness classification. *Mechanical Systems and Signal Processing*, *117*, 738–756. https://doi.org/10.1016/j.ymssp.2018.07.043

Gutowski, T. G., & Dym, C. L. (1976). Propagation of ground vibration: A review. *Journal of Sound and Vibration*, *49*(2), 179–193. https://doi.org/10.1016/0022-460x(76)90495-8

Hao, H., & Ang, T. C. (1998). Analytical modeling of traffic-induced ground vibrations. *Journal of Engineering Mechanics*, *124*(8), 921–928. https://doi.org/10.1061/(asce)0733-9399(1998)124:8(921)

Hunaidi, O., & Tremblay, M. (1997). Traffic-induced building vibrations in Montréal. *Canadian Journal of Civil Engineering*, *24*(5), 736–753. https://doi.org/10.1139/l97-023

Hunt, H. (1991). Stochastic modelling of traffic-induced ground vibration. *Journal of Sound and Vibration*, *144*(1), 53–70. https://doi.org/10.1016/0022-460x(91)90732-y

Jaeggi, D., Laurich, B., Nussbaum, C., Schuster, K., & Connolly, P. (2018). Tectonic structure of the "main fault" in the Opalinus Clay, Mont Terri Rock Laboratory (Switzerland). In *Mont Terri Rock Laboratory, 20 years* (pp. 69–86). Springer. https://doi.org/10.1007/978-3-319-70458-6_4

Kim, D.-S., & Lee, J.-S. (2000). Propagation and attenuation characteristics of various ground vibrations. *Soil Dynamics and Earthquake Engineering*, *19*(2), 115–126. https://doi.org/10.1016/s0267-7261(00)00002-6

Kumar, R., Choudhury, D., & Bhargava, K. (2016). Determination of blast-induced ground vibration equations for rocks using mechanical and geological properties. *Journal of Rock Mechanics and Geotechnical Engineering*, *8*(3), 341–349. https://doi.org/10.1016/j.jrmge.2015.10.009

Lak, M. A., Degrande, G., & Lombaert, G. (2011). The effect of road unevenness on the dynamic vehicle response and ground-borne vibrations due to road traffic. *Soil Dynamics and Earthquake Engineering*, *31*(10), 1357–1377. https://doi.org/10.1016/j.soildyn.2011.04.009

Le Gonidec, Y., Sarout, J., Wassermann, J., & Nussbaum, C. (2014). Damage initiation and propagation assessed from stress-induced microseismic events during a mine-by test in the Opalinus Clay. *Geophysical Journal International*, *198*(1), 126–139. https://doi.org/10.1093/gji/ggu122

Levin, V., & Park, J. (1997). P-SH conversions in a flat-layered medium with anisotropy of arbitrary orientation. *Geophysical Journal International*, *131*(2), 253–266. https://doi.org/10.1111/j.1365-246x.1997.tb01220.x

Li, X., Li, H., & Zhang, G. (2019). Damage assessment and blast vibrations controlling considering rock properties of underwater blasting. *International Journal of Rock Mechanics and Mining Sciences*, *121*, 104045. https://doi.org/10.1016/j.ijrmms.2019.06.004

Madshus, C., & Kaynia, A. (2000). High-speed railway lines on soft ground: Dynamic behaviour at critical train speed. *Journal of Sound and Vibration*, *231*(3), 689–701. https://doi.org/10.1006/jsvi.1999.2647

Meng, H., & Ben-Zion, Y. (2018). Characteristics of airplanes and helicopters recorded by a dense seismic array near Anza California. *Journal of Geophysical Research: Solid Earth*, *123*(6), 4783–4797. https://doi.org/10.1029/2017jb015240

Meng, H., Ben-Zion, Y., & Johnson, C. W. (2021). Analysis of seismic signals generated by vehicle traffic with application to derivation of subsurface Q-values. *Seismological Research Letters*. https://doi.org/10.1785/0220200457

Mordret, A., Brenguier, F., Causse, M., Boué, P., Voisin, C., Dumont, I., & Ampuero, J.-P. (2020). Seismic stereometry reveals preparatory behavior and source kinematics of intermediate-size earthquakes. *Geophysical Research Letters*, *47*(17), e2020GL088563. https://doi.org/10.1029/2020gl088563

Murmu, S., Maheshwari, P., & Verma, H. K. (2018). Empirical and probabilistic analysis of blast-induced ground vibrations. *International Journal of Rock Mechanics and Mining Sciences*, *103*, 267–274. https://doi.org/10.1016/j.ijrmms.2018.01.038

Nakagawa, S., Nihei, K., & Myer, L. (2000). Shear-induced conversion of seismic waves across single fractures. *International Journal of Rock Mechanics and Mining Sciences*, *37*(1–2), 203–218. https://doi.org/10.1016/s1365-1609(99)00101-x

Nateghi, R. (2011). Prediction of ground vibration level induced by blasting at different rock units. *International Journal of Rock Mechanics and Mining Sciences*, *48*(6), 899–908. https://doi.org/10.1016/j.ijrmms.2011.04.014

Nejati, H. R., Ahmadi, M., & Hashemolhosseini, H. (2012). Numerical analysis of ground surface vibration induced by underground train movement. *Tunnelling and Underground Space Technology*, *29*, 1–9. https://doi.org/10.1016/j.tust.2011.12.006

Peterson, J. R. (1993). *Observations and modeling of seismic background noise* (Technical Report). US Geological Survey. https://doi.org/10.3133/ofr93322

Ren, X., Wu, J., Tang, Y., & Yang, J. (2019). Propagation and attenuation characteristics of the vibration in soft soil foundations induced by high-speed trains. *Soil Dynamics and Earthquake Engineering*, *117*, 374–383. https://doi.org/10.1016/j.soildyn.2018.11.004

Roux, P., Sabra, K. G., Gerstoft, P., Kuperman, W., & Fehler, M. C. (2005). P-waves from cross-correlation of seismic noise. *Geophysical Research Letters*, *32*(19), L19303. https://doi.org/10.1029/2005gl023803

Ry, R. V., Cummins, P., & Widiyantoro, S. (2019). Shallow shear-wave velocity beneath Jakarta, Indonesia revealed by body-wave polarization analysis. *Geosciences*, *9*(9), 386. https://doi.org/10.3390/geosciences9090386

Snieder, R. (2002). Coda wave interferometry and the equilibration of energy in elastic media. *Physical Review E*, *66*(4), 046615. https://doi.org/10.1103/physreve.66.046615

Stähler, S. C., Sens-Schönfelder, C., & Niederleithinger, E. (2011). Monitoring stress changes in a concrete bridge with coda wave interferometry. *Journal of the Acoustical Society of America*, *129*(4), 1945–1952. https://doi.org/10.1121/1.3553226

Stehly, L., Campillo, M., & Shapiro, N. (2006). A study of the seismic noise from its long-range correlation properties. *Journal of Geophysical Research*, *111*(B10), B10306. https://doi.org/10.1029/2005jb004237

Stockwell, J. W. (1999). The CWP/SU: Seismic Unix package. *Computers & Geosciences*, *25*(4), 415–419. https://doi.org/10.1016/s0098-3004(98)00145-9

Studer, J., & Suesstrunk, A. (1981). *Swiss standard for vibrational damage to buildings*. Proceedings of the 10th International Conference on Soil Mechanics and Foundation Engineering (pp. 307–312).

Takemiya, H. (2003). Simulation of track–ground vibrations due to a high-speed train: The case of X-2000 at Ledsgard. *Journal of Sound and Vibration*, *261*(3), 503–526. https://doi.org/10.1016/s0022-460x(02)01007-6

Taniguchi, E., & Sawada, K. (1979). Attenuation with distance of traffic-induced vibrations. *Soils and Foundations*, *19*(2), 15–28. https://doi.org/10.3208/sandf1972.19.2_15

Viens, L., Denolle, M. A., Hirata, N., & Nakagawa, S. (2018). Complex near-surface rheology inferred from the response of greater Tokyo to strong ground motions. *Journal of Geophysical Research: Solid Earth*, *123*(7), 5710–5729. https://doi.org/10.1029/2018jb015697

Watts, G., & Krylov, V. (2000). Ground-borne vibration generated by vehicles crossing road humps and speed control cushions. *Applied Acoustics*, *59*(3), 221–236. https://doi.org/10.1016/s0003-682x(99)00026-2

With, C., Bahrekazemi, M., & Bodare, A. (2006). Validation of an empirical model for prediction of train-induced ground vibrations. *Soil Dynamics and Earthquake Engineering*, *26*(11), 983–990. https://doi.org/10.1016/j.soildyn.2006.03.005

Yang, J., & Sato, T. (2000). Interpretation of seismic vertical amplification observed at an array site. *Bulletin of the Seismological Society of America*, *90*(2), 275–285. https://doi.org/10.1785/0119990068

Yang, X. J. (1995). *Evaluation of man-made ground vibrations*. Paper presented at the Third International Conference on Recent Advances in Geotechnical Earth Engineering and Soil Dynamics.

Yu, K., Gu, X., Huang, M., Ma, X., & Li, N. (2021). Experimental, numerical and analytical studies on the attenuation of maglev train-induced vibrations with depth in layered soils. *Soil Dynamics and Earthquake Engineering*, *143*, 106628. https://doi.org/10.1016/j.soildyn.2021.106628

Zhang, Y., Li, Y. E., & Ku, T. (2019). Geotechnical site investigation for tunneling and underground works by advanced passive surface wave survey. *Tunnelling and Underground Space Technology*, *90*, 319–329. https://doi.org/10.1016/j.tust.2019.05.003